






RESEARCH ARTICLE

10.1029/2021JA030196

Electron Diffusion by Magnetosonic Waves in the Earth's Radiation Belts

Jin-Mann Wong¹ , Nigel P. Meredith¹ , Richard B. Horne¹ , Sarah A. Glauert¹ , and Johnathan P. J. Ross¹ 

¹British Antarctic Survey, Natural Environment Research Council, Cambridge, UK

Key Points:

- Pitch angle diffusion rates for magnetosonic waves exceed those of hiss and VLF transmitters over energy-dependent ranges of pitch angles
- Magnetosonic waves have a significant effect on electron loss timescales in the region $2.0 \leq L^* \leq 3.5$
- Magnetosonic waves reduce the loss timescales during active times from 140.4 to 35.7 days for 1 MeV electrons at $L^* = 2.0$

Correspondence to:

J.-M. Wong,
jinnng@bas.ac.uk

Citation:

Wong, J.-M., Meredith, N. P., Horne, R. B., Glauert, S. A., & Ross, J. P. J. (2022). Electron diffusion by magnetosonic waves in the Earth's radiation belts. *Journal of Geophysical Research: Space Physics*, 127, e2021JA030196. <https://doi.org/10.1029/2021JA030196>

Received 8 DEC 2021
Accepted 11 FEB 2022

Abstract We conduct a global survey of magnetosonic waves and compute the associated bounce- and drift-averaged diffusion coefficients, taking into account colocated measurements of $f_{pe}f_{ce}$, to assess the role of magnetosonic waves in radiation belt dynamics. The average magnetosonic wave intensities increase with increasing geomagnetic activity and decreasing relative frequency with the majority of the wave power in the range $f_{cp} < f < 0.3f_{LHR}$ during active conditions. In the region $4.0 \leq L^* \leq 5.0$, the bounce- and drift-averaged energy diffusion rates due to magnetosonic waves never exceed those due to whistler mode chorus, suggesting that whistler mode chorus is the dominant mode for electron energization to relativistic energies in this region. Further in, in the region $2.0 \leq L^* \leq 3.5$, the bounce- and drift-averaged pitch angle diffusion rates due to magnetosonic waves can exceed those due to plasmaspheric hiss and very low frequency (VLF) transmitters over energy-dependent ranges of intermediate pitch angles. We compute electron lifetimes by solving the 1D pitch angle diffusion equation including the effects of plasmaspheric hiss, VLF transmitters, and magnetosonic waves. We find that magnetosonic waves can have a significant effect on electron loss timescales in the slot region reducing the loss timescales during active times from 5.6 to 1.5 days for 500 keV electrons at $L^* = 2.5$ and from 140.4 to 35.7 days for 1 MeV electrons at $L^* = 2.0$.

Plain Language Summary The modeling and forecasting of the Earth's radiation belts, composed of charged particles trapped by the Earth's magnetic field, is important for mitigating damage to satellites during extreme solar events. Interactions with plasma waves in the magnetosphere can energize and scatter these charged particles, depending on the intensity of the plasma wave and local plasma conditions. One such plasma wave is the magnetosonic wave, which can contribute to both electron energization and loss to the atmosphere. In this paper, we study the role of magnetosonic waves using simultaneous measurements of their intensity and local plasma conditions and find a reduction in the loss timescales of high energy electrons in the near-Earth region when magnetosonic waves act in combination with other plasma waves.

1. Introduction

The Earth's radiation belts were discovered over 60 years ago, at the beginning of the space age (Van Allen, 1959; Van Allen & Frank, 1959), and have since been extensively studied by many spacecraft. However, questions remain regarding the relative importance of the physical processes controlling their behavior. The inner radiation belt, which lies in the region $1.1 < L^* < 2.0$ is relatively stable, except during the largest geomagnetic storms (Baker et al., 2007). In contrast, the outer radiation belt, which typically lies in the region $3.0 < L^* < 8.0$, is highly dynamic. The inner and outer belts are usually separated by a slot region which is devoid of relativistic electrons but which can become filled during exceptionally strong storms (Baker et al., 2007). In the outer radiation belt, the flux of relativistic electrons can vary by orders of magnitude on timescales ranging from minutes to weeks (Baker et al., 1994). This variability is due to a variety of acceleration, transport, and loss processes, all of which become amplified during enhanced geomagnetic activity (Li & Hudson, 2019). Understanding this variability is important since enhanced fluxes of these so-called “killer” electrons can damage satellites (Iucci et al., 2005; Wrenn, 1995; Wrenn et al., 2002) and pose a risk to humans in space.

Magnetosonic waves, one of the most intense emissions in the inner magnetosphere, may interact strongly with electrons and ions. Indeed, it has been suggested that magnetosonic waves can contribute to both the acceleration and loss of relativistic electrons (Horne et al., 2007; Meredith et al., 2008), although the overall significance of the waves on radiation belt dynamics remains to be determined.

©2022. The Authors.

This is an open access article under the terms of the [Creative Commons Attribution License](https://creativecommons.org/licenses/by/4.0/), which permits use, distribution and reproduction in any medium, provided the original work is properly cited.

Magnetosonic waves are right-hand polarized whistler mode waves with frequencies between the proton gyrofrequency, f_{cp} , and the lower hybrid resonance frequency, f_{LHR} . They were first observed by Russell et al. (1969), using data from the search coil magnetometer on OGO 3 within 2° of the magnetic equator, and observed to propagate perpendicular to the external magnetic field in the equatorial plane. Subsequent studies have shown that the waves are primarily observed within 5° of the magnetic equator and occur over a broad radial extent, between 2 and $8 R_E$, both inside and outside the plasmopause (Chen et al., 2010; Gurnett, 1976; Laakso et al., 1990; Ma et al., 2013, 2016; Meredith et al., 2008; Němec et al., 2005; Perraut et al., 1982; Santolík et al., 2004; Zou et al., 2019). The intensities of the waves increase with increasing geomagnetic activity (Kim & Shprits, 2017; Ma et al., 2013, 2016; Meredith et al., 2008; Zou et al., 2019), suggesting that the waves are related to periods of enhanced convection and/or substorm activity.

Simultaneous wave and particle observations, together with instability calculations, show that the waves can be generated by unstable proton ring distributions at energies of ~ 10 keV (Boardsen et al., 1992; Horne et al., 2000). Indeed, proton ring distributions at these energies have been observed in association with magnetosonic waves throughout the inner magnetosphere, both inside and outside the plasmopause (Boardsen et al., 1992; Kim & Shprits, 2018; Meredith et al., 2008; Perraut et al., 1982; Yuan et al., 2018). Once generated, the waves can become trapped in azimuthal propagation around the plasmopause by steep local density gradients if generated outside the plasmopause (Kasahara et al., 1994). In this region, Landau damping by plasma sheet electrons restricts the waves to latitudes close to the magnetic equator (Horne et al., 2000), consistent with observations.

Local pitch angle and energy diffusion coefficients for magnetosonic waves were computed in Horne et al. (2007), using an observation of magnetosonic waves on Cluster 3 in November 2002. A peak wave amplitude of 218 pT was observed resulting in energy acceleration timescales outside the plasmopause of order of 1 day for MeV electrons. However, diffusion coefficients computed using average wave intensities have since resulted in much slower acceleration timescales. For example, Shprits et al. (2013), using a model of magnetosonic waves based on wave statistics from two frequency channels of the THEMIS Search Coil Magnetometer Filter Bank data and two representative values of f_{pe}/f_{ce} , estimated energy acceleration timescales in excess of 30 days for electrons with energies in the range $1 < E < 3$ MeV both inside and outside of the plasmopause. More recently, Ma et al. (2016), using the analytical formula of Bortnik et al. (2015) together with Van Allen Probe wave statistics and density models inside and outside the plasmopause (Sheeley et al., 2001), determined a peak energy acceleration timescale in excess of 10 days outside the plasmopause.

Plasmaspheric hiss, lightning-generated whistlers, and very low frequency (VLF) transmitters all contribute to electron loss in the slot region (Abel & Thorne, 1998; Meredith et al., 2007, 2009; Ripoll et al., 2014; Ross et al., 2019). For MeV electrons, the dominant contributor to pitch angle scattering is plasmaspheric hiss, which has pitch angle diffusion rates that dip around pitch angles of 70° . Acting on their own, this would result in a bottleneck and, at $L = 2.0$, result in MeV electron loss timescales which are much longer than observed (Meredith et al., 2009). However, this bottleneck can potentially be removed when other wave modes such as lightning-generated whistlers and magnetosonic waves are included (Meredith et al., 2009), suggesting that magnetosonic waves could play a role in electron loss in the slot region (Meredith et al., 2009; Mourenas et al., 2013).

Diffusion rates have traditionally been computed using geomagnetic-activity-dependent global models of the average wave spectra and average ratio of the plasma frequency to the electron gyrofrequency, f_{pe}/f_{ce} . The importance of capturing the variability of f_{pe}/f_{ce} in chorus acceleration of MeV electrons was shown in Agapitov et al. (2019), where analytical estimates of bounce-averaged MeV electron diffusion rates were computed using local f_{pe}/f_{ce} values and mean wave spectra. More recent studies have shown that it is important to include both the variability of the wave spectra and the plasma properties in radiation belt modeling (Agapitov et al., 2020; Ross et al., 2020, 2021; Watt et al., 2019). Watt et al. (2019) showed that the mean pitch angle diffusion coefficients, D_{aa} , for plasmaspheric hiss calculated by averaging the D_{aa} from colocated and simultaneous measurements of the wave power and f_{pe}/f_{ce} were larger than those calculated from average values of the wave power and f_{pe}/f_{ce} . Due to the large computation time required to compute diffusion coefficients, Watt et al. (2019) restricted their study to selected spatial location bins. By employing approximate analytical estimates of MeV electron pitch angle diffusion coefficients, Agapitov et al. (2020) computed, using simultaneous local measurements of wave spectra and f_{pe}/f_{ce} , bounce-averaged MeV electron pitch angle diffusion coefficients due to plasmaspheric hiss as a function of L^* , magnetic local time (MLT), and AE.

Ross et al. (2020) took this concept forward and showed that diffusion coefficients for EMIC waves calculated by combining the effects of individual wave spectra and plasma properties resulted in diffusion over a wider range of energies and pitch angles and significantly improved the agreement between the calculated decay of relativistic electrons and Van Allen Probe data when compared against existing diffusion models based on average wave spectra and plasma properties. In particular, the modeled fluxes during periods of decay were well captured, having been typically overestimated by a factor of 10 by the original method. The value of f_{pe}/f_{ce} is also important for wave–particle interactions with magnetosonic waves. For example, the Landau resonance at any given energy shifts to larger pitch angles with increasing f_{pe}/f_{ce} and the peak diffusion rates occur at decreasing energy with increasing f_{pe}/f_{ce} (Horne et al., 2007). These results suggest that a comprehensive treatment of diffusion rates due to magnetosonic waves should also include the variability of the wave spectra and the plasma properties.

In this paper, we use data from the EMFISIS instrument on Van Allen Probe A (Mauk et al., 2013) to compute bounce- and drift-averaged diffusion coefficients for magnetosonic waves using this new approach, taking into account colocated measurements of the wave power and f_{pe}/f_{ce} . We also combine the bounce- and drift-averaged pitch angle diffusion rates with those due to plasmaspheric hiss and VLF transmitters to study the effect of magnetosonic waves on electron loss timescales in the region $2.0 \leq L^* \leq 3.5$. The instrumentation and data analysis techniques used to develop the wave model are described in Section 2. The global morphology of the average intensities of magnetosonic waves as a function of spatial location, geomagnetic activity, and relative frequency is presented in Section 3. The bounce- and drift-averaged pitch angle and energy diffusion coefficients are presented in Section 4 and the electron loss timescales described in Section 5. Finally, the results are discussed and our conclusions presented in Sections 6 and 7, respectively.

2. Instrumentation and Data Analysis

2.1. Instrumentation

The Van Allen Probes were launched on 30 August 2012 into highly elliptical orbits with a perigee of $\sim 1.1R_E$, an apogee of $\sim 5.8R_E$, and an inclination of 10° (Mauk et al., 2013). The satellites each had an orbital period of approximately 9 hr and swept through the inner magnetosphere approximately 5 times per day, making them ideally suited to study magnetosonic waves in this important region. In this study, we use 7 years of data from the EMFISIS instrument (Kletzing et al., 2013) on Van Allen Probe A between 26 October 2012, after the complete deployment of the electric field booms, and the end of the mission on 14 October 2019.

The wave magnetic field spectral density and polarization properties, calculated by the singular value decomposition method (Santolik et al., 2003), were provided by the waveform receiver (WFR). This instrument measured the vector wave electric and magnetic fields in the frequency range from 2.1 Hz to 11.2 kHz, covering the frequency range of magnetosonic waves in the inner magnetosphere. The electron plasma frequency, f_{pe} , provided as a Level 4 data product, was derived from the high-frequency receiver (HFR), which measured the wave electric field spectral density in the frequency range 10–487 kHz. When visible it was derived from the upper hybrid frequency, f_{UHR} , and elsewhere by the lower frequency limit of the continuum radiation (Kurth et al., 2015). The electron gyrofrequency was determined directly from the 1s fluxgate magnetometer measurements of the local magnetic field.

2.2. Data Analysis

We first excluded data collected during thruster firings, periods of eclipse, and charging events. We also excluded intervals when the fluxgate magnetometer data were flagged as invalid, in calibration mode or in magFill mode. We then removed the instrumental background noise from the valid data using the technique described in Malaspina et al. (2017). This method involves fitting a Gaussian to the power spectral density distribution of the lowest frequency band of the WFR to derive a signal-to-noise ratio that is then applied to the other frequencies. In particular, the signal-to-noise ratio is given by

$$r_{sn} = \frac{\mu + 2\sigma}{\mu}, \quad (1)$$

where μ and σ are the mean and standard deviation of the Gaussian fit. The threshold for frequency band i , with noise peak n_i , is then given by

$$t_i = r_{sn}n_i, \quad (2)$$

where measurements below t_i in frequency band i are excluded.

We identify magnetosonic waves from the WFR data by restricting to frequencies between the proton gyrofrequency and the lower hybrid resonance frequency, $f_{cp} < f < f_{LHR}$, and imposing a large wave normal angle, $\psi > 80^\circ$, and near-linear ellipticity $|e| \leq 0.2$, which are characteristic of magnetosonic waves (Russell et al., 1969; Santolík et al., 2004).

Since radiation belt models generally use coordinate systems based on the adiabatic invariants, we use the magnetic coordinates L^* , MLT, and magnetic latitude to study the data. These were computed using the TS04 (Tsyganenko & Sitnov, 2005) models and the IGRF field at the middle of the appropriate year. Since L^* is designed for particles and we are using it for waves, we assume a local pitch angle of 90° in the calculation of L^* . This is justified as magnetosonic waves usually interact with electrons at large pitch angles (Horne et al., 2007). The models are also parameterized by geomagnetic activity indices such as the *AE* and *Kp* indices. Current radiation belt forecasting models use the *Kp* index due to the requirement of a 24 hr forecast of the driving index and, consequently, we use this index in our study.

Examples of strong magnetosonic wave activity observed by the EMFISIS instrument on Van Allen Probe A on 1 January 2015 are shown in Figure 1. Here, strong magnetosonic waves are observed below the lower hybrid resonance frequency on three separate occasions, from 04:00 to 04:30, 07:50 to 09:20, and 20:40 to 21:50 (Figures 1e and 1f). These waves are all associated with large wave normal angles (Figure 1d) and low ellipticities (Figure 1c), confirming that they are magnetosonic waves (Figure 1f). Note that the strong wave power at the lowest frequencies observed throughout this interval (Figure 1b) is background noise that has been successfully removed by the background subtraction (Figure 1e). This demonstrates that the background subtraction is essential in order to correctly identify the waves. Other instances of strong wave power below the lower hybrid resonance frequency during this interval are associated with smaller wave normal angles and larger ellipticities. These events all occur inside the plasmopause and are identified as plasmaspheric hiss (Figure 1f). The strong magnetosonic waves were all observed close to the magnetic equator (Figure 1g) inside the plasmopause as evidenced by the lack of ECH waves in the HFR data (Meredith et al., 2004; Figure 1a).

To study the frequency dependence of the intensity of the magnetosonic waves, we rebin the wave power spectral density into frequency bands varying with the lower hybrid resonance frequency. We use 10 frequency bands between f_{cp} and f_{LHR} of width $0.1f_{LHR}$, except the lowest frequency band which spans $f_{cp} < f < 0.1f_{LHR}$. The proton gyrofrequency can lie below the 2 Hz lower frequency limit of the WFR instrument when $L^* > 4$. As a result, a fraction of magnetosonic wave intensity in the lowest frequency band $f_{cp} < f < 0.1f_{LHR}$ is missed in this analysis for $L^* > 4$. Since this L^* value is greater than the $2 \leq L^* \leq 3.5$ range that is studied in Section 5, the missed power will not affect the results on electron lifetimes. Furthermore, only a small fraction of the magnetosonic wave power is missed in this analysis for $L^* < 5.25$. For $|\lambda_m| < 6^\circ$, in the bins $3.75 \leq L^* < 4.25$ and $4.75 \leq L^* < 5.25$, f_{cp} less than 2 Hz occurs 0.02% and 4.2% of the time, respectively, and the average fraction of the lowest frequency band not accounted for is 0.02 and 0.03, respectively. This small fraction of missing wave power will have an insignificant effect on the comparison with the chorus diffusion coefficients at $L^* = 4$ and $L^* = 5$ in Section 4.3.

3. Global Morphology

3.1. MLT Distribution

Figure 2 presents the global distribution of the average wave intensity of magnetosonic waves in the frequency ranges $0.6f_{LHR} < f < 0.7f_{LHR}$ (Figures 2a–2c) and $f_{cp} < f < 0.1f_{LHR}$ (Figures 2d–2f) in the equatorial region, $|\lambda_m| < 6^\circ$, for, from left to right increasing levels of geomagnetic activity as monitored by the *Kp* index. The average intensities are computed by averaging the wave intensity of each individual observation in each geomagnetic activity and relevant spatial location bin, taking into account times when magnetosonic waves are not observed. The maps extend linearly out to $L^* = 7.0$ with noon at the top and dawn to the right. The average intensities are shown in the large panels and the corresponding sampling distributions are shown in the small panels. In the lowest frequency

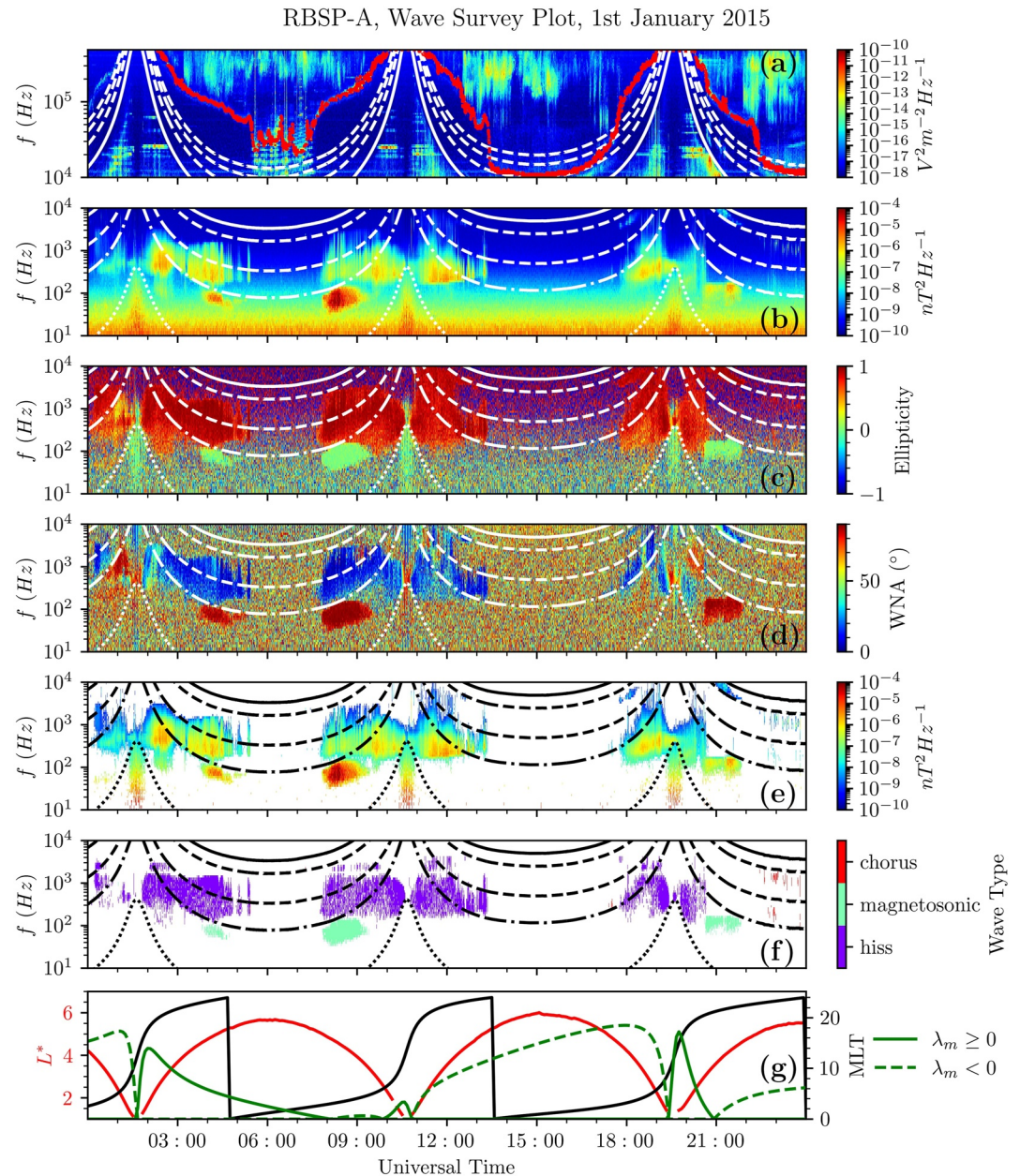


Figure 1. Survey plot showing the magnetospheric waves observed by the Van Allen Probe A EMFISIS instrument on 1 January 2015. (a) The wave electric field spectral density as measured by the high frequency receiver (HFR). Here, the solid red line denotes f_{UHR} and the solid and dashed white lines represent the electron gyrofrequency, f_{ce} , and its harmonics. (b) The wave magnetic field spectral density as measured by the waveform receiver (WFR) and (c, d) the derived ellipticity and wave normal angle. (e) The WFR magnetic field spectral density with measurements below the noise threshold removed and (f) the wave classification, where magnetosonic waves appear in cyan. In (b)–(f), the solid line represents f_{ce} , the dashed lines $0.5f_{ce}$ and $0.1f_{ce}$, the dash-dot line f_{LHR} , and the dotted line f_{cp} . The position of the spacecraft in magnetic coordinates is shown in (g).

band (Figures 2d–2f), the wave intensities increase with increasing geomagnetic activity and are strongest during active conditions with average intensities typically exceeding 1,000 pT² in the region $1.5 < L^* < 3.0$ from 06:00 through noon to 22:00 MLT, extending to higher L^* in the afternoon sector (Figure 2f). The intensities also generally increase with increasing geomagnetic activity in the $0.6f_{LHR} < f < 0.7f_{LHR}$ but the intensities are much weaker (Figures 2a–2c) and the effect is not as significant as in the lower frequency band. These results are consistent with previous studies showing that average magnetosonic wave intensities increase with increasing geomagnetic activity (Kim & Shprits, 2017; Ma et al., 2013, 2016; Meredith et al., 2008; Zou et al., 2019).

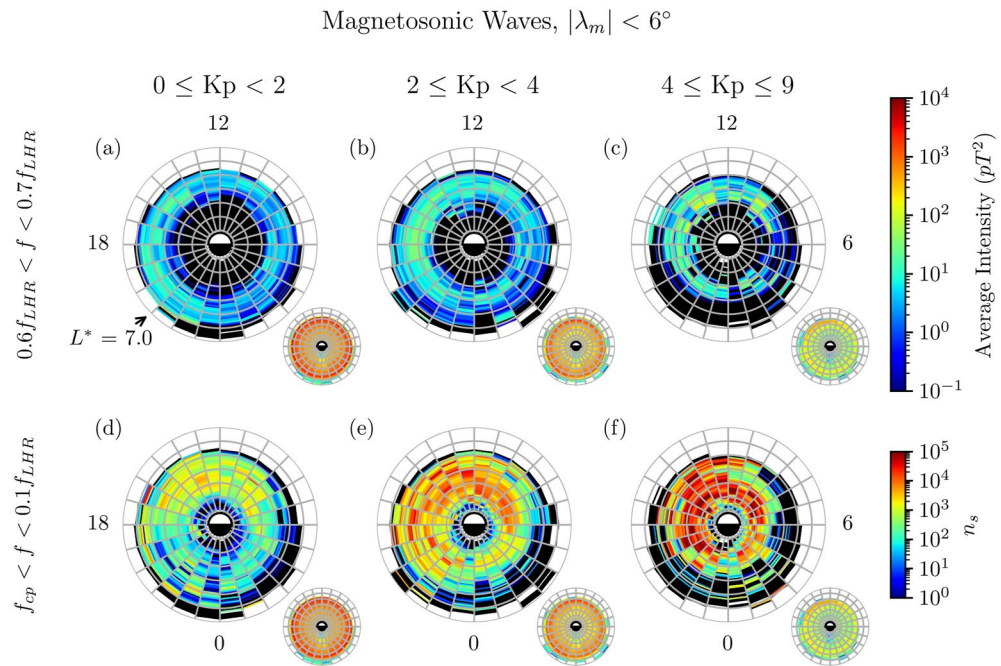


Figure 2. Global maps of the average wave intensity of magnetosonic waves in the relative frequency bands $0.6f_{LHR} < f < 0.7f_{LHR}$ (a–c) and $f_{cp} < f < 0.1f_{LHR}$ (d–f) in the near equatorial region, $|\lambda_m| < 6^\circ$, as a function of L^* and magnetic local time (MLT) for, from left to right, increasing geomagnetic activity as monitored by Kp. The maps extend linearly out to $L^* = 7.0$ with noon at the top and dawn to the right. The average intensities are shown in the large panels and the corresponding sampling distributions are shown in the small panels.

We investigate the frequency dependence of the global distribution of magnetosonic waves further in Figure 3. Here, we plot the global distribution of the average wave intensity of magnetosonic waves in nine frequency bands between f_{cp} and $0.9f_{LHR}$ in the equatorial region, $|\lambda_m| < 6^\circ$, during geomagnetically active conditions, $4 \leq Kp \leq 9$ in the same format as Figure 2. In the lowest frequency band, $f_{cp} < f < 0.1f_{LHR}$, strong waves, which we define as those with intensities greater than 200 pT^2 , are observed in the region $1.5 < L^* < 3.0$ over most MLT, the exception being a 2 hr MLT sector around midnight, and extend to higher L^* , $3.0 < L^* < 5.0$, on the dusk-side, primarily in the region $12 < \text{MLT} < 20$ (Figure 3i). Strong waves are also observed in the frequency bands $0.1f_{LHR} < f < 0.2f_{LHR}$ and $0.2f_{LHR} < f < 0.3f_{LHR}$, where they are primarily observed in the region $2.0 < L^* < 4.0$ from 08 to 20 MLT, extending to higher L^* , $4.0 < L^* < 5.0$, near noon, $10 < \text{MLT} < 15$ (Figures 3g and 3h). The extent and magnitude of the waves decrease with increasing frequency, with strong waves rarely being observed on average in frequency bands greater than $0.3f_{LHR} < f < 0.4f_{LHR}$ (Figures 3a–3e).

3.2. Latitudinal Distribution

The latitudinal dependence of the magnetosonic waves in the nine frequency bands displayed in Figure 3 is shown in Figure 4. Here, the average magnetosonic wave intensities, averaged over all MLT, during active conditions, $4 \leq Kp \leq 9$, are plotted in the meridional plane. The average intensities are plotted in the large panels and the corresponding sampling distributions in the small panels. To aid visualization of the data, dipole field lines and lines of constant magnetic latitude are included on the plot. The waves are confined to the equatorial region with the bulk of the wave power observed at magnetic latitudes less than 6° . The strong waves in the lowest frequency band have the largest latitudinal extent, extending up to 6° in the region $2.0 < L^* < 3.5$ (Figure 4i). The latitudinal extent of the strong waves decreases with increasing frequency, where they become primarily restricted to within a few degrees of the equator in the $0.2f_{LHR} < f < 0.3f_{LHR}$ frequency band (Figure 4g). Strong waves are less common at higher frequencies and are largely absent in frequency bands above $0.3f_{LHR} < f < 0.4f_{LHR}$.

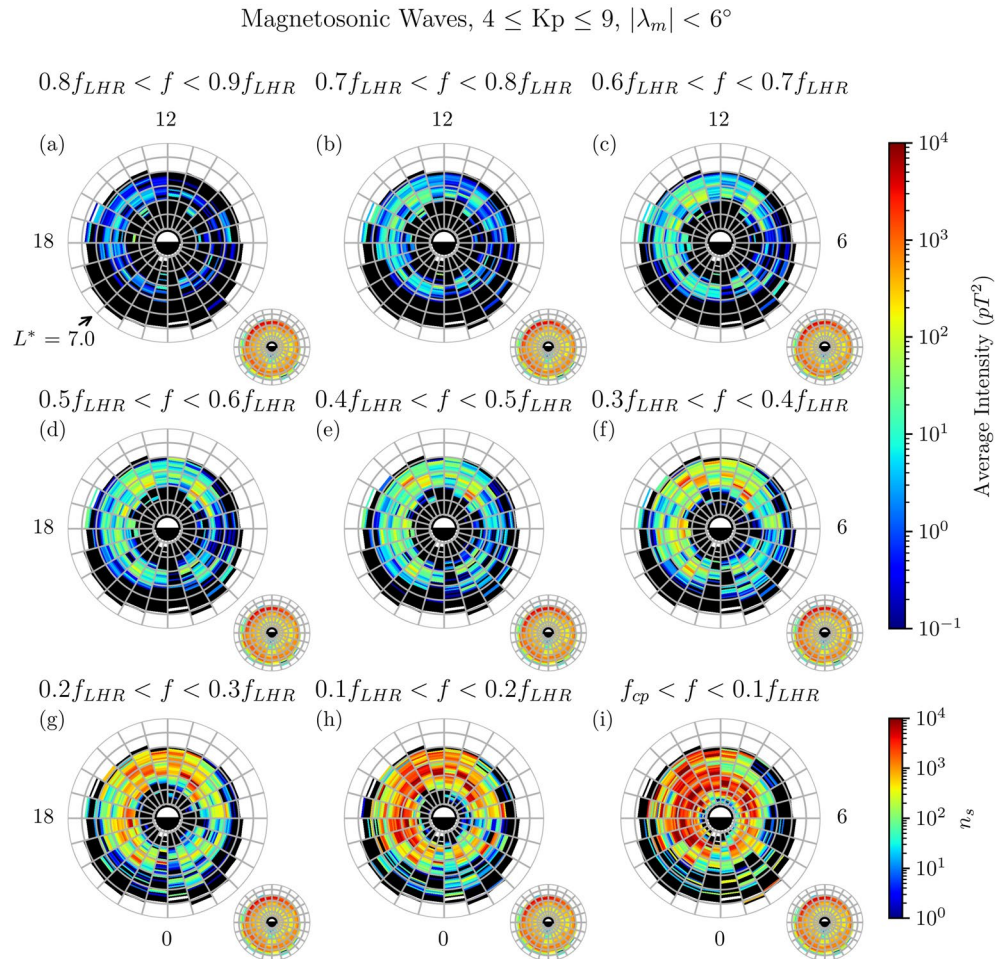


Figure 3. Global maps of the average wave intensity of magnetosonic waves in the near-equatorial region, $|\lambda_m| < 6^\circ$, during active conditions, $4 \leq Kp \leq 9$, as a function of L^* and MLT for nine relative frequency bands between f_{cp} and $0.9f_{LHR}$. The maps extend linearly out to $L^* = 7.0$ with noon at the top and dawn to the right. The average intensities are shown in the large panels and the corresponding sampling distributions are shown in the small panels.

4. Diffusion Coefficients

4.1. Computation Method

We calculate the pitch angle and energy diffusion coefficients using a data-driven version of the PADIE code (Glauert & Horne, 2005; Ross et al., 2021), taking into account the power spectral density profile of the magnetosonic waves and colocated measurements of f_{pe}/f_{ce} as described in Ross et al. (2021). Here, the electron plasma frequency is determined from the HFR electric field data (Kurth et al., 2015). However at low L^* , the upper hybrid resonance frequency often exceeds the upper frequency limit of the HFR instrument and, consequently, f_{pe} cannot be determined. To compute the diffusion coefficients at low L^* , $L^* < 2.2$, we use the empirical density model in Ozhogin et al. (2012) to compute f_{pe}/f_{ce} when electron density measurements are not available.

In order to calculate the diffusion coefficients using the method in Ross et al. (2021), we bin the average wave intensity and corresponding number of samples in each relative frequency band as a function of L^* , MLT, λ_m , f_{pe}/f_{ce} , and geomagnetic activity as recorded by the Kp index. We adopt ten L^* bins in the range $1.25 \leq L^* \leq 6.25$ in steps of $0.5 L^*$, 24 MLT bins in steps of 1 hr of MLT, 4 latitudinal bins in the range $-6^\circ \leq \lambda_m \leq 6^\circ$ in steps of 3° , and 16 bins of f_{pe}/f_{ce} in the range $1 \leq f_{pe}/f_{ce} \leq 41$ in steps of 2.5. The geomagnetic activity is divided into five bins as follows, $0 \leq Kp < 1$, $1 \leq Kp < 2$, $2 \leq Kp < 3$, $3 \leq Kp < 4$, and $4 \leq Kp \leq 9$, which are a balance between having sufficient samples for good statistics and resolution. Bins with less than 100 samples are excluded from the computation of diffusion coefficients due to having poor statistics.

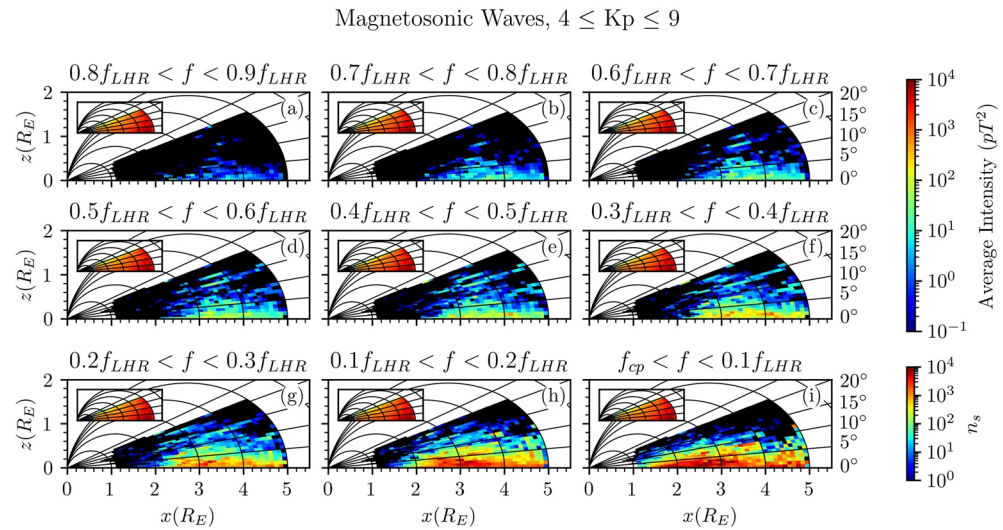


Figure 4. Global maps of the average wave intensity of magnetosonic waves in the meridional plane during active conditions, $4 \leq Kp \leq 9$, for nine relative frequency bands between f_{cp} and $0.9f_{LHR}$. To aid visualization of the data, dipole field lines and lines of constant magnetic latitude are included on the plots. The average intensities are shown in the large panels and the corresponding sampling distributions in the small panels. Measurements with $L^* > 5.0$ are omitted due to absence of full MLT data coverage.

The variability of the wave power spectral density is examined Figure 5. Here, the MLT-averaged wave power spectral density in the region $|\lambda_m| < 3^\circ$ is plotted as a function of relative frequency and f_{pe}/f_{ce} during quiet, intermediate, and active conditions for $2.5 \leq L^* < 3.5$, Figures 5a, 5d and 5g, $3.5 \leq L^* < 4.5$, Figures 5b, 5e and 5h, and $4.5 \leq L^* < 5.5$, Figures 5c, 5f and 5i. The MLT averaging is carried out by first averaging within each 1 hr MLT bin and then averaging across the 24 MLT bins. The average wave power in each f_{pe}/f_{ce} bin, obtained by

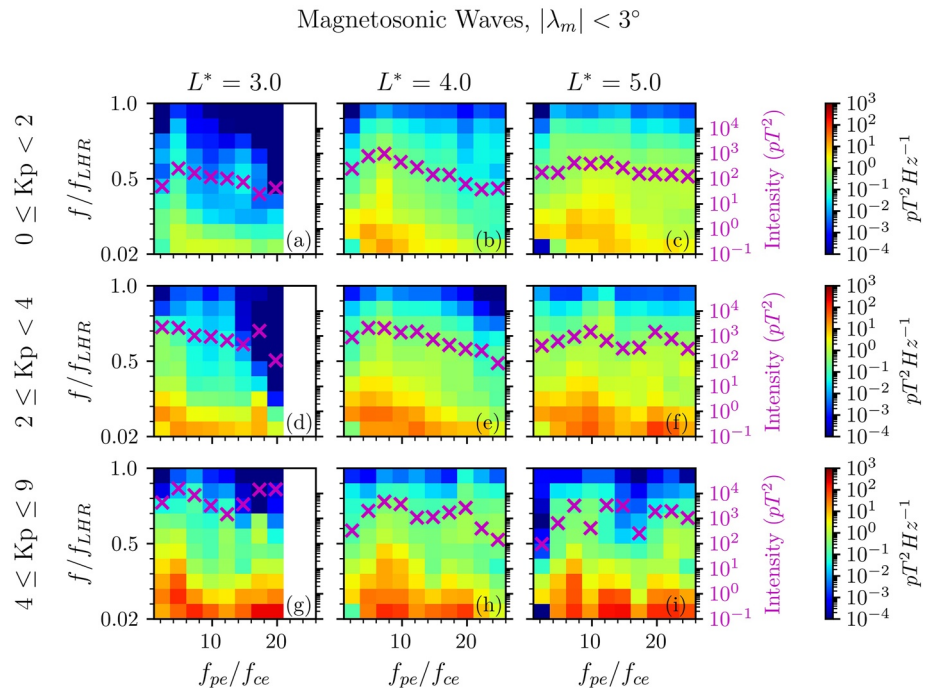


Figure 5. MLT-averaged magnetosonic wave power spectral density in the near equatorial region, $|\lambda_m| < 3^\circ$, during quiet, intermediate, and active times, as a function of relative frequency and f_{pe}/f_{ce} for $2.5 \leq L^* < 5.5$. The magenta crosses plot the average magnetosonic wave power over the full frequency range $f_{cp} < f < f_{LHR}$ in each f_{pe}/f_{ce} bin.

integrating over the full frequency range, is plotted in the magenta crosses. For all L^* , we observe the general trend of the wave power spectral densities increasing with decreasing relative frequency for all values of f_{pe}/f_{ce} . As the activity level increases from quiet to active conditions, the wave power in each f_{pe}/f_{ce} bin generally increases, evident also from the intensification of the wave power spectral density in the lower frequency bands.

At $L^* = 3$ during quiet conditions, Figure 5a, the peak wave power spectral density occurs for $6 \leq f_{pe}/f_{ce} < 8.5$ and falls off rapidly with increasing frequency. Moving to intermediate and active conditions, Figures 5d and 5g, strong wave power spectral densities, which we define as those greater than $5 \text{ pT}^2 \text{ Hz}^{-1}$ and coded orange or red in the plots, occur over a wider range of f_{pe}/f_{ce} values, with the highest spectral densities being observed during active conditions. Note, the lack of measurements for $f_{pe}/f_{ce} > 21$ at $L^* = 3$ is due to the upper frequency limit of the HFR instrument. For $L^* = 4$ and $L^* = 5$, the same trend is observed with the strongest wave power spectral densities being seen during active conditions for a wide range of values of f_{pe}/f_{ce} .

For $L^* = 4$ and $L^* = 5$, we also observe the strong wave power spectral densities extending to higher frequencies at lower values of f_{pe}/f_{ce} . For example, in Figure 5e, where strong wave power spectral densities only occur in the lowest frequency band for $16 \leq f_{pe}/f_{ce} < 23.5$ but extend up to $0.3f_{LHR}$ in the range $3.5 \leq f_{pe}/f_{ce} < 8.5$. Although generally extending over a smaller frequency range, the strong wave power spectral densities occurring at large f_{pe}/f_{ce} can give rise to wave power comparable to that observed at low f_{pe}/f_{ce} values. Similar to increasing f_{pe}/f_{ce} , increasing the wave frequency has the effect of shifting the Landau resonance to higher pitch angles for any given energy.

We subsequently calculate the bounce-averaged pitch angle and energy diffusion rates, $\langle D_{aa} \rangle$ and $\langle D_{EE} \rangle$, as a function of pitch angle and energy in each L^* , MLT, and geomagnetic activity bin. This is done first by computing the weighted average of the diffusion coefficients over f_{pe}/f_{ce} in a given spatial location and geomagnetic activity bin. The resulting coefficients are then bounce averaged by summing the diffusion coefficients from each associated magnetic latitude bin. We assume an electron–proton plasma and the wave normal angle distribution in Horne et al. (2007), given by a Gaussian in $X = \tan \psi$, with the peak at $\psi = 89^\circ$ and width $\tan 86^\circ$. The resulting coefficients are drift averaged by averaging the bounce-averaged coefficients over the 24 MLT bins to obtain diffusion coefficients, $\langle D_{aa} \rangle^D$ and $\langle D_{EE} \rangle^D$, as a function of L^* , geomagnetic activity, energy, and pitch angle.

4.2. Number of Resonances

The effect of incorporating resonances beyond the Landau resonance was investigated for a range of f_{pe}/f_{ce} and L^* for different energies. We found that including only the Landau resonance misses out both energy and pitch angle diffusion at low pitch angles for energies $\geq 4 \text{ MeV}$, with the higher order resonances having a larger effect on the pitch angle diffusion coefficients. The importance of higher order resonances increases with both f_{pe}/f_{ce} and electron energy above 4 MeV. From computing the diffusion coefficients for electron energies of 4 and 10 MeV and two f_{pe}/f_{ce} values, 3 and 30, for resonances $n = -j, \dots, j$, where $j = 1, \dots, 10$, we concluded that including resonances $n = -7, \dots, 7$ gives a good compromise between obtaining accurate diffusion coefficients and computation time. The contributions from resonances $|n| > 7$ decreases with n and test runs with $n = -70, \dots, 70$ showed differences between the diffusion coefficients of order $< 10^{-10} \text{ s}^{-1}$ from the $n = -7, \dots, 7$ calculations.

4.3. Results

The bounce- and drift-averaged diffusion coefficients are plotted as a function of pitch angle and energy in Figure 6 for, from left to right, increasing L^* , during quiet (Figures 6a–6h) and active conditions (Figures 6i–6p). In each set of two panels, the pitch angle diffusion coefficients are presented in the upper panel and the energy diffusion coefficients in the lower panel. The pitch angle and energy diffusion rates are dominated by those caused by the Landau resonance with the influence of the cyclotron resonances only becoming apparent for pitch angle diffusion at the lowest pitch angles and highest energies (Figures 6c, 6d and 6j–6l). For any given energy, there tends to be a range of pitch angles where the diffusion due to the Landau resonance is strongest with the lower and upper pitch angle bounds extending to higher pitch angles with increasing energy.

During quiet conditions, the pitch angle diffusion rates generally increase with increasing L^* with rates peaking around $2 \times 10^{-7} \text{ s}^{-1}$ for energies in the range $100 \text{ keV} < E < 200 \text{ keV}$ at pitch angles in the range $70^\circ < \alpha_{eq} < 80^\circ$

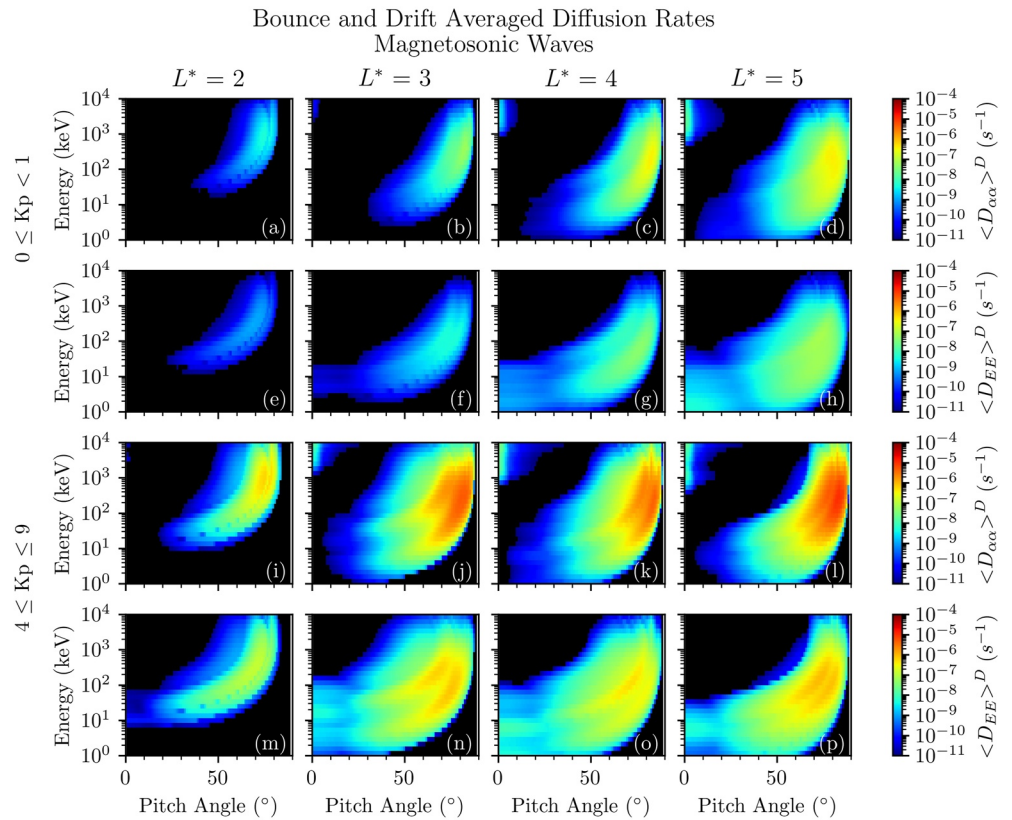


Figure 6. Bounce- and drift-averaged magnetosonic wave pitch angle and energy diffusion coefficients for $Kp < 1$ (a–h) and $4 \leq Kp \leq 9$ (i–p) for, from left to right, increasing L^* .

at $L^* = 5.0$ (Figure 6d). The energy diffusion coefficients follow a similar trend, albeit with lower rates, peaking $5 \times 10^{-8} \text{ s}^{-1}$ at $L^* = 5.0$ in a similar region of energy, pitch angle space (Figure 6h).

The diffusion coefficients are larger and more significant during active conditions. The same general trends are observed but the peak pitch angle diffusion rates now exceed $5 \times 10^{-6} \text{ s}^{-1}$ for energies in the range $100 \text{ keV} < E < 500 \text{ keV}$ at pitch angles in the range $65^\circ < \alpha_{eq} < 85^\circ$ at $L^* = 5.0$ (Figure 6l). The results show that there is no pitch angle diffusion into the loss cone from the 90° pitch angle either during quiet or active times. However, pitch angle scattering into the loss cone at low pitch angles is possible for energies $> 1 \text{ MeV}$, although the rates are very small, being no larger than 10^{-7} s^{-1} during active conditions. The energy diffusion coefficients follow a similar trend, whilst remaining lower than the corresponding pitch angle diffusion rates, peaking around 10^{-6} s^{-1} at $L^* = 5.0$ in a similar region of energy, pitch angle space (Figure 6p).

During both quiet and active conditions, we observe that the energy diffusion coefficients can be greater than the pitch angle diffusion coefficients for energies $< 100 \text{ keV}$. This feature is also seen in the magnetosonic diffusion coefficients in Ma et al. (2016), obtained using the analytical formula derived in Bortnik and Thorne (2010). Although it is uncommon for energy diffusion to exceed pitch angle diffusion at a given energy and pitch angle, this is not forbidden and it is checked in PADIE that the coefficients satisfy the inequality

$$D_{\alpha E}^2 < D_{\alpha\alpha} D_{EE}, \quad (3)$$

derived in Lyons (1974).

The bounce- and drift-averaged energy diffusion rates due to magnetosonic waves during active times, $Kp = 4$, are compared with the chorus diffusion coefficients in Horne et al. (2013) in Figure 7. The chorus diffusion matrix in Horne et al. (2013) uses the Olson–Pfitzer quiet time external magnetic field model (Olson & Pfitzer, 1977) and therefore the L^* values in their diffusion matrix do not directly correspond to those in this paper. Nonetheless, we can still make a useful comparison. On average, the energy diffusion rates for magnetosonic waves are lower

Bounce and Drift Averaged Diffusion Rates, Kp = 4

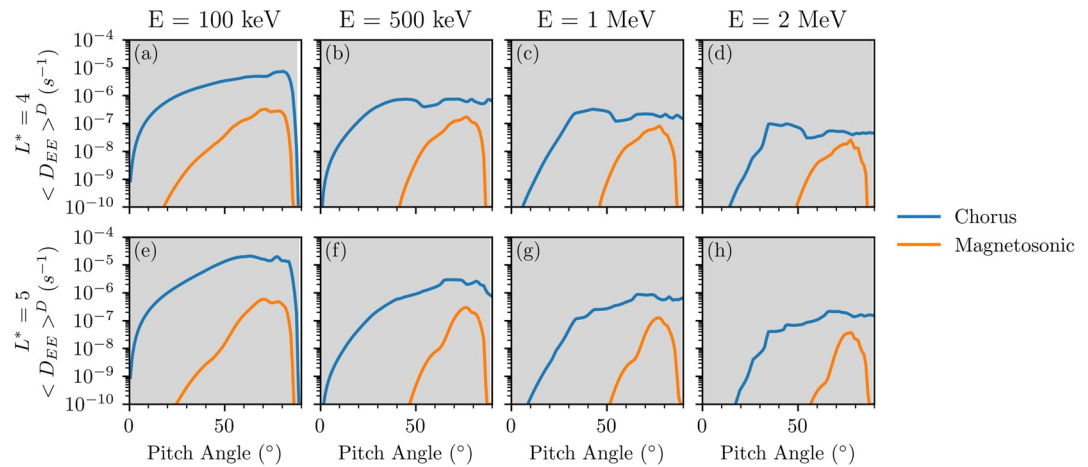


Figure 7. Bounce- and drift-averaged energy diffusion rates of magnetosonic waves (orange) and whistler mode chorus (blue) during active times, Kp = 4, as a function of pitch angle at $L^* = 4.0$ (a–d) and $L^* = 5.0$ (e–h), for, from left to right, increasing energy.

than those due to chorus waves at all energies at both $L^* = 4.0$ and 5.0 . This suggests that electron energization to relativistic energies will, on average, be dominated by whistler mode chorus with magnetosonic waves playing a minor role.

The results in Figure 6 show that magnetosonic waves alone cannot scatter electrons from a pitch angle of 90° into the loss cone. However, the pitch angle diffusion rates become large at intermediate pitch angles where they may assist pitch angle scattering due to other wave modes and, potentially, decrease electron loss timescales when acting in combination with plasmaspheric hiss (Meredith et al., 2009). In the next section, we combine the bounce- and drift-averaged pitch angle diffusion rates with those due to plasmaspheric hiss and VLF transmitters to study, in detail, the effect of magnetosonic waves on electron loss timescales in the region $2.0 \leq L^* \leq 3.5$.

5. Loss Timescales

In this section, we investigate the effect of magnetosonic waves on electron loss timescales in the presence of plasmaspheric hiss and VLF transmitters, focusing on the slot region where these waves could be important. For plasmaspheric hiss, we use the diffusion matrix derived from a database of plasma waves in the frequency range 10 Hz to 4 kHz compiled from eight satellites (Meredith et al., 2018) and which includes contributions from lightning-generated whistlers in the frequency range $2 \text{ kHz} < f < 4 \text{ kHz}$ (e.g., Meredith et al., 2006). For VLF transmitters, we use the diffusion matrix computed in Ross et al. (2019) from global models of VLF transmitters derived from Van Allen Probe observations (Meredith et al., 2019). We also include scattering from Coulomb collisions using the prescription in Abel and Thorne (1998) and the density model in Ross et al. (2019). Similarly to the chorus diffusion matrix discussed in Section 4.3, the matrices listed above use the Olson–Pfizer magnetic field model (Olson & Pfizer, 1977). However, for the region of interest in this section, $2 \leq L^* \leq 3.5$, the difference between L^* computed with Olson–Pfizer and TS04 (Tsyganenko & Sitnov, 2005) is expected to be small.

The pitch angle diffusion coefficients during active conditions, Kp = 4, are shown as a function of pitch angle for magnetosonic waves (green traces), plasmaspheric hiss (blue traces), and VLF transmitters (orange traces) for, from left to right, increasing energy and, from top to bottom, increasing L^* in Figure 8. Here, the white regions highlight the range of pitch angles where the pitch angle diffusion rates due to magnetosonic waves dominate over those due to plasmaspheric hiss and VLF transmitters. At $L^* = 2.0$, magnetosonic waves increase the pitch diffusion rates by a factor of 10 or more over a range of pitch angles, for all energies considered. In particular, at MeV energies, they help fill in bottlenecks in the pitch angle diffusion rates due to plasmaspheric hiss (Figures 8a–8d). Moving out, at higher values of L^* , magnetosonic waves remain important at lower energies but become insignificant at 2 MeV.

Bounce and Drift Averaged Diffusion Rates, Kp = 4

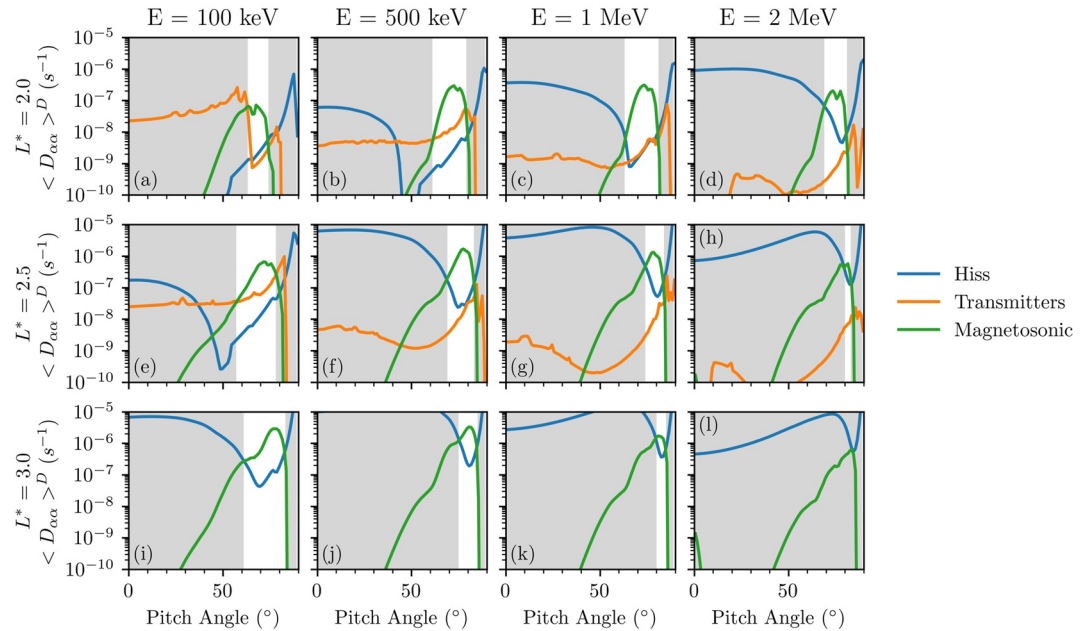


Figure 8. Bounce- and drift-averaged pitch angle diffusion rates of plasmaspheric hiss (blue), very low frequency (VLF) transmitters (orange), and magnetosonic waves (green) during active conditions, Kp = 4, for, from left to right, increasing energy and, from top to bottom, increasing L^* . White regions highlight the pitch angle range where the pitch angle diffusion rates of magnetosonic waves exceed that of plasmaspheric hiss and VLF transmitters.

In general, the pitch angle distribution evolves into a characteristic shape, which then decays with a characteristic timescale that can be determined. Using the 1D pitch angle diffusion model described in Ross et al. (2019), we study the impact of magnetosonic waves on electron loss timescales after a steady rate of decay in the flux has been reached. The 1D model solves the pitch angle diffusion equation neglecting energy and radial diffusion, which are expected to be small in comparison to pitch angle scattering in the region $2.0 \leq L^* \leq 3.5$, with a numerical time stepping method for fixed boundary conditions

$$\frac{\partial f_{\alpha=0^\circ}(t)}{\partial t} = \frac{\partial f_{\alpha=90^\circ}(t)}{\partial t} = 0, \quad (4)$$

where $f_\alpha(t)$ is the flux at pitch angle α and time t (Meredith et al., 2009; Ross et al., 2019). Electron losses into the atmosphere via Coulomb collisions are included within the bounce loss cone via a loss term with a timescale of a quarter bounce period. For all runs, we include pitch angle diffusion from Coulomb collisions, plasmaspheric hiss, and VLF transmitters and impose that a steady decay rate in the pitch angle distribution has been reached when the decay rate at each pitch angle is within 2% of the average decay rate across all pitch angles. The initial pitch angle distribution, $f_\alpha(t = 0)$, is taken to be

$$f_\alpha(t = 0) \propto \sin^3 \alpha. \quad (5)$$

The pitch angle distribution varies with energy, spatial location, and geomagnetic activity and the exponent of 3 was chosen following the $\sin^n \alpha$ fits in Shi et al. (2016) for the region $2 \leq L^* \leq 3.5$. The shape of the initial distribution is also forgotten once the pitch angle distribution has evolved into its characteristic shape. The decay rate at time t and pitch angle α , τ_α , is computed from

$$f_\alpha(t) = f_\alpha(t - \Delta t) e^{-\Delta t / \tau_\alpha}, \quad (6)$$

where Δt is the time step.

Figure 9 presents the loss timescales with and without magnetosonic waves for Kp = 2.5 (Figures 9a–9d) and Kp = 4.0 (Figures 9e–9h) for, from left to right, increasing energy. Here, the loss timescales with and without

Loss Timescales with and without Magnetosonic Waves

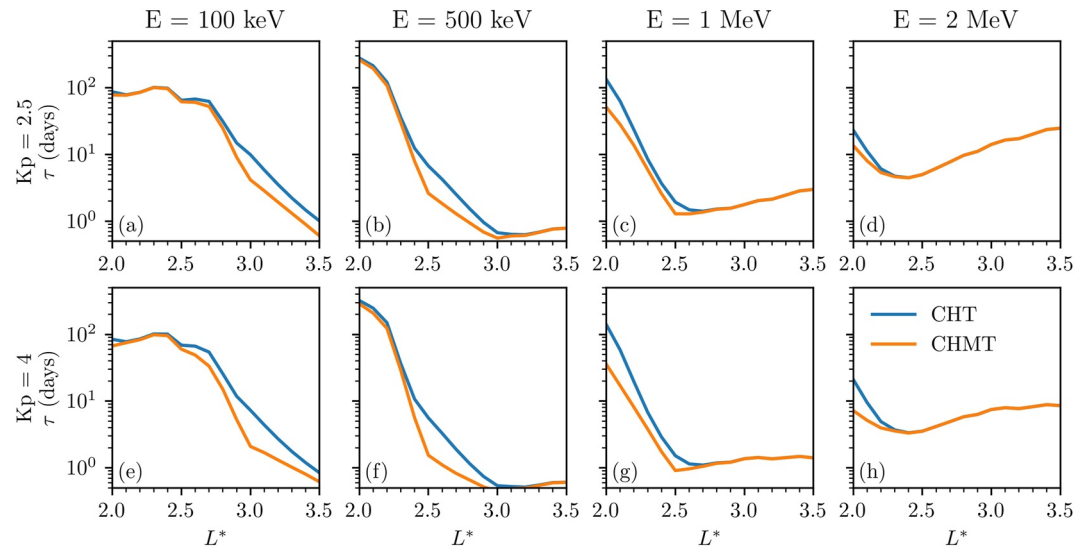


Figure 9. Loss timescales, in days, for 1D model runs with (orange) and without (blue) magnetosonic waves for $K_p = 2.5$ (a–d) and $K_p = 4$ (e–h), for, from left to right, increasing energy.

magnetosonic waves are colored orange and blue, respectively. Magnetosonic waves result in the reduction of the electron lifetimes over a range of L^* for each energy at both intermediate at high activity levels, with the reductions being largest during active conditions. For example, during intermediate conditions, the presence of magnetosonic waves reduces the loss timescales for 500 keV electrons from 6.7 to 2.6 days and for 1 MeV electrons from 133.6 to 51.1 days at $L^* = 2.5$ and 2.0, respectively (Figures 9b and 9c). The effects are even more significant during active conditions when magnetosonic waves reduce the loss timescales for 500 keV electrons from 5.6 to 1.5 days and for 1 MeV electrons from 140.4 to 35.7 days at $L^* = 2.5$ and 2.0, respectively (Figures 9f and 9g).

The ratio of loss timescales between the model runs without and with magnetosonic waves is shown in Figure 10. Here, this ratio is plotted as a function of L^* for, quiet, intermediate, and active conditions for, from left to right, increasing energy. The largest reductions, of the order of a factor of 4, are seen during active conditions at $L^* = 2.5$ and $L^* = 2.0$ for 500 keV (Figure 10b, red trace) and 1 MeV electrons (Figure 10c, red trace), respectively. During intermediate conditions, at 100 keV, decreases in the loss timescales, of the order 1.5 or more, are observed in the region $2.9 \leq L^* \leq 3.5$ (Figure 10a, orange trace). Moving to higher energies, the region where magnetosonic waves decrease the timescales by a factor of 1.5 or more moves to lower L^* , being observed in

Ratio of Loss Timescales

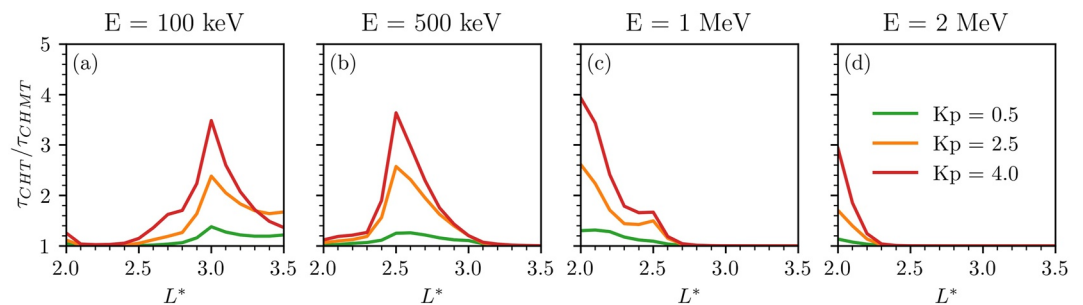


Figure 10. Ratio of loss timescales obtained from 1D model runs without (CHT) and with (CHMT) the inclusion of magnetosonic waves for three K_p values for, from left to right, increasing energy. The effect of magnetosonic waves is largest at high geomagnetic activity, peaking for lower energies at increasing L^* .

the region $2.4 \leq L^* \leq 2.8$ at 500 keV (Figure 10b, orange trace) and in the region $2.0 \leq L^* \leq 2.2$ at 1 MeV (Figure 10c, orange trace). Magnetosonic waves become even more important during active conditions where reductions in the lifetimes by a factor of 2 or more are observed in the regions $2.9 \leq L^* \leq 3.2$, $2.5 \leq L^* \leq 2.7$, and $2.0 \leq L^* \leq 2.2$ at 100 keV, 500 keV, and 1 MeV, respectively (Figures 10a–10c, red traces).

6. Discussion

Horne et al. (2007) suggested that magnetosonic waves could accelerate electrons to relativistic energies on a timescale of the order of 1 day outside the plasmopause and could thus be an important acceleration mechanism in the Earth's outer radiation belt. However, more recently, both Shprits et al. (2013) and Ma et al. (2016) have suggested that the timescales could be an order of magnitude or more larger. Our results show that the bounce- and drift-averaged energy diffusion rates for magnetosonic waves are always lower than those due to chorus waves in the important energy range from 100 keV to 2 MeV at $L^* = 4.0$ and 5.0. This suggests that electron energization to relativistic energies is dominated by whistler mode chorus with magnetosonic waves playing a very minor role, at least during average conditions. This is in contrast to the suggestion that magnetosonic waves could be very important for electron acceleration to relativistic energies. Horne et al. (2007) used a peak wave intensity of $47,000 \text{ pT}^2$ based on observations from Cluster 3 in November 2002. This intensity is much larger than the average intensities of 2,866 and 2,620 pT^2 at $L^* = 4.0$ and 5.0, respectively, in the near equatorial region, $|\lambda_m| < 6^\circ$, during active conditions $4 \leq Kp \leq 9$ determined from our global model. Since diffusion rates are proportional to the magnetic field intensity, Figure 7 shows that the energy diffusion by magnetosonic waves would be 16–18 times larger than average in this case for ranges of intermediate pitch angles at energies greater than 500 keV. Indeed, the Van Allen Probe observations show that such large intensities are observed, with total wave intensities in the region $|\lambda_m| < 6^\circ$ exceeding $47,000 \text{ pT}^2$ for 2.4% of all the positive identifications of magnetosonic waves. This suggests that while whistler mode chorus plays the dominant role in the energization of electrons to relativistic energies most of the time, there could be cases when the magnetosonic waves are particularly strong and persistent and magnetosonic waves play the dominant role.

Meredith et al. (2009) suggested that both lightning-generated whistlers and magnetosonic waves at $L = 2.0$ could significantly reduce the lifetimes of 2 MeV electrons, potentially bringing the lifetimes down from 238 days for plasmaspheric hiss alone to 34 days when lightning-generated whistlers were included and to 43 days when magnetosonic waves during active conditions were included. However, these results were based on diffusion rates derived from wave electric field measurements from the Plasma Wave Experiment (Anderson et al., 1992) on board the CRRES spacecraft (Johnson & Kierein, 1992) and were subject to a potentially inaccurate conversion from the wave electric field to the wave magnetic field. Furthermore, the magnetosonic wave observations included contributions from plasmaspheric hiss occurring in the same frequency range as the magnetosonic waves. Here, we use wave magnetic field observations of plasmaspheric hiss and magnetosonic waves, noting that our definition of plasmaspheric hiss also includes contributions from lightning-generated whistlers in the frequency range $2 \text{ kHz} < f < 4 \text{ kHz}$. Furthermore, the waves in the frequency range $f_{cp} < f < f_{LHR}$ have been clearly identified as magnetosonic waves by applying the additional criteria of large wave normal angles and low ellipticity. By using the computed diffusion rates in the 1D pitch angle diffusion equation, our results show a significant reduction in the electron lifetimes in the presence of magnetosonic waves, maximizing for 500 keV electrons at $L^* = 2.5$ and for 1 MeV electrons at $L^* = 2.0$ where the modeled lifetimes are reduced from 5.6 to 1.5 days and from 140.4 to 35.7 days, respectively, during active conditions.

To understand whether pitch angle diffusion driven by magnetosonic waves results in a better agreement with measurements, we compare our results with the e -folding lifetimes derived in Claudepierre et al. (2020). In their study, Claudepierre et al. (2020) computed lifetimes for the decay of electron fluxes over a minimum period of 5 days using data from the MAGEIS instrument (Blake et al., 2013) on the Van Allen Probes. Their paper focuses on electrons with equatorial pitch angle between 70° and 110° , in contrast to the loss timescales computed here, for the decay of the flux once a steady rate of decay has been reached, which has no pitch angle dependence. For the energies and L^* values in Table 1 and our choice of initial pitch angle distribution, the fluxes from the 1D pitch angle scattering model for pitch angles between 70° and 110° often decay slower before reaching the steady decay rate and the model values in Table 1 can be treated as lower bounds on the loss timescale in the comparison. The model of lightning-generated whistlers incorporated in the hiss diffusion matrix only includes frequencies below 4 kHz and a comprehensive treatment would include the effects of lightning-generated whistlers above

Table 1

Comparison of Electron Loss Timescales From the 1D Model Runs With and Without Magnetosonic Waves for Quiet, Intermediate, and Active Conditions, and the Lifetimes Determined in Claudepierre et al. (2020), Labeled C2020

Energy and L^*	Loss timescale (days)						
	Without magnetosonic			With magnetosonic			C2020
	Kp = 0.5	Kp = 2.5	Kp = 4	Kp = 0.5	Kp = 2.5	Kp = 4	
500 keV, $L^* = 2.5$	12.6	6.7	5.6	10.1	2.6	1.5	7
1 MeV, $L^* = 2.0$	120.2	133.6	140.4	92.3	51.1	35.7	50

Note. All timescales in the table are expressed in units of days.

4 kHz (Agapitov et al., 2014; Green et al., 2020; Ma et al., 2017; Záhlava et al., 2019). However, a deep minimum in the diffusion rates due to hiss and lightning-generated whistlers still exists even when the higher frequencies are included (Agapitov et al., 2014) and, in such circumstances, the diffusion driven by magnetosonic waves reported here will continue to act to fill the bottleneck resulting in a subsequent reduction in the computed electron loss timescales.

Table 1 shows the electron loss timescales for 500 keV and 1 MeV at three activity levels and the empirical lifetimes obtained in Claudepierre et al. (2020). The empirical lifetimes are likely to result from a combination of the modeled lifetimes for different Kp levels and while we do not expect a value of Kp = 4 to be sustained over a period of 5 days we present the result to show the lifetimes that can be achieved with the model during active conditions. The observed loss timescale of 7 days for 500 keV electrons at $L^* = 2.5$ falls in the range of the modeled lifetimes during quiet and intermediate conditions for the scenarios both with and without magnetosonic waves. However, the observed loss timescale of 50 days for 1 MeV electrons is shorter by more than a factor of 2 than that estimated from plasmaspheric hiss and VLF transmitters alone, even during active conditions, and the latter is a lower bound. In this case, magnetosonic waves are required to bring the lifetimes down to observable levels.

The Ozhogin et al. (2012) density model is used to compute $f_{pe}f_{ce}$ when density measurements from the Van Allen Probes are not available for $L^* < 2.2$ and accounts for 78.6% of the $f_{pe}f_{ce}$ values in the $L^* = 2$ bin. The magnetosonic diffusion coefficients for $L^* = 2$ therefore do not capture the full variability of $f_{pe}f_{ce}$. Model runs with a magnetosonic diffusion matrix computed using only Ozhogin et al. (2012) density values produced a lifetime of 42.8 days for 1 MeV electrons at $L^* = 2$ and Kp = 4 compared with 35.7 days with the current method. This suggests that electron lifetimes at $L^* = 2$ could reduce further if the full variability of $f_{pe}f_{ce}$ is taken into account.

7. Conclusions

We have conducted a global survey of magnetosonic waves and computed bounce- and drift-averaged diffusion coefficients, taking into account colocated measurements of the wave power and $f_{pe}f_{ce}$. Using these diffusion coefficients, we have computed electron lifetimes from running a 1D pitch angle diffusion model with plasmaspheric hiss, VLF transmitters, and magnetosonic waves. Our principal findings are as follows:

1. The average magnetosonic wave intensities increase with increasing geomagnetic activity and decreasing relative frequency with the majority of the wave power in the range $f_{cp} < f < 0.3f_{LHR}$ during active conditions.
2. The bounce- and drift-averaged energy diffusion rates in the region $4.0 \leq L^* \leq 5.0$ are lower than those due to whistler mode chorus, suggesting that whistler mode chorus is the dominant mode for electron energization to relativistic energies.
3. The bounce- and drift-averaged pitch angle diffusion rates exceed those due to plasmaspheric hiss and VLF transmitters over a limited range of intermediate pitch angles in the region $2.0 \leq L^* \leq 3.5$.
4. Magnetosonic waves have a significant effect on electron loss timescales in the slot region reducing the loss timescales from 6.7 to 2.6 days for 500 keV electrons at $L^* = 2.5$ and from 133.6 to 51.1 days for 1 MeV electrons at $L^* = 2.0$ during intermediate conditions.

The results from this paper have shown that magnetosonic waves can contribute to electron loss timescales at low L^* and should be incorporated into quasi-linear theory based global radiation belt models.

Data Availability Statement

The results and data shown in this paper are available to download from the U.K. Polar Data Centre at <https://doi.org/10.5285/aae6ea2f-7dab-4ab1-830f-a4c53589e340>.

Acknowledgments

We acknowledge the NASA Van Allen Probes and Craig Kletzing for use of the EMFISIS data, available online (<https://emfisis.physics.uiowa.edu/data/index>). We also acknowledge the Radiation Belt Storm Probes ECT Science Operations and Data Center for the provision of the magnetic ephemeris data, available online (<https://www.rbsp-ect.lanl.gov/data-pub/rbspa/MagEphem/>). We thank the NSSDC Omniweb for the provision of the Kp indices used in this paper. The research leading to these results has received funding from the Natural Environment Research Council (NERC) Highlight Topic grant NE/P01738X/1 (Rad-Sat) and the NERC grants NE/V00249X/1 (Sat-Risk) and NE/R016038/1.

References

- Abel, B., & Thorne, R. M. (1998). Electron scattering loss in Earth's inner magnetosphere: 2. Sensitivity to model parameters. *Journal of Geophysical Research*, *103*(A2), 2397–2407. <https://doi.org/10.1029/97JA02920>
- Agapitov, O. V., Artemyev, A. V., Mourenas, D., Kasahara, Y., & Krasnoselskikh, V. (2014). Inner belt and slot region electron lifetimes and energization rates based on Akebono statistics of whistler waves. *Journal of Geophysical Research: Space Physics*, *119*, 2876–2893. <https://doi.org/10.1002/2014JA019886>
- Agapitov, O. V., Mourenas, D., Artemyev, A., Claudepierre, S. G., Hospodarsky, G., & Bonnell, J. W. (2020). Lifetimes of relativistic electrons as determined from plasmaspheric hiss scattering rates statistics: Effects of ω_{pe}/ω_{ce} and wave frequency dependence on geomagnetic activity. *Geophysical Research Letters*, *47*, e2020GL088052. <https://doi.org/10.1029/2020GL088052>
- Agapitov, O. V., Mourenas, D., Artemyev, A., Hospodarsky, G., & Bonnell, J. (2019). Time scales for electron quasi-linear diffusion by lower-band chorus waves: The effects of ω_{pe}/ω_{ce} dependence on geomagnetic activity. *Geophysical Research Letters*, *46*, 6178–6187. <https://doi.org/10.1029/2019GL083446>
- Anderson, R. R., Gurnett, D. A., & Odem, D. L. (1992). CRRES plasma wave experiment. *Journal of Spacecraft and Rockets*, *29*(4), 570–573. <https://doi.org/10.2514/3.25501>
- Baker, D. N., Blake, J. B., Callis, L. B., Cummings, J. R., Hovestadt, D., Kanekal, S., et al. (1994). Relativistic electron acceleration and decay time scales in the inner and outer radiation belts: SAMPEX. *Geophysical Research Letters*, *21*(6), 409–412. <https://doi.org/10.1029/93GL03532>
- Baker, D. N., Kanekal, S. G., Horne, R. B., Meredith, N. P., & Glauert, S. A. (2007). Low-altitude measurements of 2–6 MeV electron trapping lifetimes at $1.5 \leq L \leq 2.5$. *Geophysical Research Letters*, *34*, L20110. <https://doi.org/10.1029/2007GL031007>
- Blake, J. B., Carranza, P. A., Claudepierre, S. G., Clemmons, J. H., Crain, W. R., Dotan, Y., et al. (2013). The magnetic electron ion spectrometer (MagEIS) instruments aboard the radiation belt storm probes (RBSP) spacecraft. *Space Science Reviews*, *179*(1), 383–421. <https://doi.org/10.1007/s11214-013-9991-8>
- Boardsen, S. A., Gallagher, D. L., Gurnett, D. A., Peterson, W. K., & Green, J. L. (1992). Funnel-shaped, low-frequency equatorial waves. *Journal of Geophysical Research*, *97*(A10), 14967–14976. <https://doi.org/10.1029/92JA00827>
- Bortnik, J., & Thorne, R. M. (2010). Transit time scattering of energetic electrons due to equatorially confined magnetosonic waves. *Journal of Geophysical Research*, *115*, A07213. <https://doi.org/10.1029/2010JA015283>
- Bortnik, J., Thorne, R. M., Ni, B., & Li, J. (2015). Analytical approximation of transit time scattering due to magnetosonic waves. *Geophysical Research Letters*, *42*, 1318–1325. <https://doi.org/10.1002/2014GL026710>
- Chen, L., Thorne, R. M., Jordanova, V. K., & Horne, R. B. (2010). Global simulation of magnetosonic wave instability in the storm time magnetosphere. *Journal of Geophysical Research*, *115*, A11222. <https://doi.org/10.1029/2010JA015707>
- Claudepierre, S. G., Ma, Q., Bortnik, J., O'Brien, T. P., Fennell, J. F., & Blake, J. B. (2020). Empirically estimated electron lifetimes in the Earth's radiation belts: Van Allen Probe observations. *Geophysical Research Letters*, *47*, e2019GL086053. <https://doi.org/10.1029/2019GL086053>
- Glauert, S. A., & Horne, R. B. (2005). Calculation of pitch angle and energy diffusion coefficients with the PADIE code. *Journal of Geophysical Research*, *110*, A04206. <https://doi.org/10.1029/2004JA010851>
- Green, A., Li, W., Ma, Q., Shen, X.-C., Bortnik, J., & Hospodarsky, G. B. (2020). Properties of lightning generated whistlers based on Van Allen Probes observations and their global effects on radiation belt electron loss. *Geophysical Research Letters*, *47*, e2020GL089584. <https://doi.org/10.1029/2020GL089584>
- Gurnett, D. A. (1976). Plasma wave interactions with energetic ions near the magnetic equator. *Journal of Geophysical Research*, *81*(16), 2765–2770. <https://doi.org/10.1029/JA081i016p02765>
- Horne, R. B., Kersten, T., Glauert, S. A., Meredith, N. P., Boscher, D., Sicard-Piet, A., et al. (2013). A new diffusion matrix for whistler mode chorus waves. *Journal of Geophysical Research: Space Physics*, *118*, 6302–6318. <https://doi.org/10.1002/jgra.50594>
- Horne, R. B., Thorne, R. M., Glauert, S. A., Meredith, N. P., Pokhotelov, D., & Santolík, O. (2007). Electron acceleration in the Van Allen radiation belts by fast magnetosonic waves. *Geophysical Research Letters*, *34*, L17107. <https://doi.org/10.1029/2007GL030267>
- Horne, R. B., Wheeler, G. V., & Alleyne, H. S. C. K. (2000). Proton and electron heating by radially propagating fast magnetosonic waves. *Journal of Geophysical Research*, *105*(A12), 27597–27610. <https://doi.org/10.1029/2000JA000018>
- Iucci, N., Levitin, A. E., Belov, A. V., Eroshenko, E. A., Ptitsyna, N. G., Villaresi, G., & Yanke, V. G. (2005). Space weather conditions and spacecraft anomalies in different orbits. *Space Weather*, *3*, S01001. <https://doi.org/10.1029/2003SW000056>
- Johnson, M. H., & Kierein, J. (1992). Combined release and radiation effects satellite (CRRES): Spacecraft and mission. *Journal of Spacecraft and Rockets*, *29*(4), 556–563. <https://doi.org/10.2514/3.55641>
- Kasahara, Y., Kenmochi, H., & Kimura, I. (1994). Propagation characteristics of the ELF emissions observed by the satellite Akebono in the magnetic equatorial region. *Radio Science*, *29*(4), 751–767. <https://doi.org/10.1029/94RS00445>
- Kim, K.-C., & Shprits, Y. (2017). Dependence of the amplitude of magnetosonic waves on the solar wind and ae index using Van Allen Probes. *Journal of Geophysical Research: Space Physics*, *122*, 6022–6034. <https://doi.org/10.1002/2017JA024094>
- Kim, K.-C., & Shprits, Y. (2018). Survey of the favorable conditions for magnetosonic wave excitation. *Journal of Geophysical Research: Space Physics*, *123*, 400–413. <https://doi.org/10.1002/2017JA024865>
- Kletzing, C. A., Kurth, W. S., Acuna, M., MacDowall, R. J., Torbert, R. B., Averkamp, T., et al. (2013). The electric and magnetic field instrument suite and integrated science (EMFISIS) on RBSP. *Space Science Reviews*, *179*(1), 127–181. <https://doi.org/10.1007/s11214-013-9993-6>
- Kurth, W. S., De Pascuale, S., Faden, J. B., Kletzing, C. A., Hospodarsky, G. B., Thaller, S., & Wygant, J. R. (2015). Electron densities inferred from plasma wave spectra obtained by the waves instrument on Van Allen Probes. *Journal of Geophysical Research: Space Physics*, *120*, 904–914. <https://doi.org/10.1002/2014JA020857>

- Laakso, H., Junginger, H., Roux, A., Schmidt, R., & de Villedary, C. (1990). Magnetosonic waves above $f_c(H^+)$ at geostationary orbit: GEOS 2 results. *Journal of Geophysical Research*, *95*(A7), 10609–10621. <https://doi.org/10.1029/JA095iA07p10609>
- Li, W., & Hudson, M. (2019). Earth's Van Allen radiation belts: From discovery to the Van Allen Probes era. *Journal of Geophysical Research: Space Physics*, *124*, 8319–8351. <https://doi.org/10.1029/2018JA025940>
- Lyons, L. R. (1974). Pitch angle and energy diffusion coefficients from resonant interactions with ion–cyclotron and whistler waves. *Journal of Plasma Physics*, *12*(3), 417–432. <https://doi.org/10.1017/S002237780002537X>
- Ma, Q., Li, W., Thorne, R. M., & Angelopoulos, V. (2013). Global distribution of equatorial magnetosonic waves observed by THEMIS. *Geophysical Research Letters*, *40*, 1895–1901. <https://doi.org/10.1002/grl.50434>
- Ma, Q., Li, W., Thorne, R. M., Bortnik, J., Kletzing, C. A., Kurth, W. S., & Hospodarsky, G. B. (2016). Electron scattering by magnetosonic waves in the inner magnetosphere. *Journal of Geophysical Research: Space Physics*, *121*, 274–285. <https://doi.org/10.1002/2015JA021992>
- Ma, Q., Mourenas, D., Li, W., Artemyev, A., & Thorne, R. M. (2017). VLF waves from ground-based transmitters observed by the Van Allen Probes: Statistical model and effects on plasmaspheric electrons. *Geophysical Research Letters*, *44*, 6483–6491. <https://doi.org/10.1002/2017GL073885>
- Malaspina, D. M., Jaynes, A. N., Hospodarsky, G., Bortnik, J., Ergun, R. E., & Wygant, J. (2017). Statistical properties of low-frequency plasmaspheric hiss. *Journal of Geophysical Research: Space Physics*, *122*, 8340–8352. <https://doi.org/10.1002/2017JA024328>
- Mauk, B. H., Fox, N. J., Kanekal, S. G., Kessel, R. L., Sibeck, D. G., & Ukhorskiy, A. (2013). Science objectives and rationale for the radiation belt storm probes mission. *Space Science Reviews*, *179*(1), 3–27. <https://doi.org/10.1007/s11214-012-9908-y>
- Meredith, N. P., Horne, R. B., & Anderson, R. R. (2008). Survey of magnetosonic waves and proton ring distributions in the Earth's inner magnetosphere. *Journal of Geophysical Research*, *113*, A06213. <https://doi.org/10.1029/2007JA012975>
- Meredith, N. P., Horne, R. B., Clilverd, M. A., Horsfall, D., Thorne, R. M., & Anderson, R. R. (2006). Origins of plasmaspheric hiss. *Journal of Geophysical Research*, *111*, A09217. <https://doi.org/10.1029/2006JA011707>
- Meredith, N. P., Horne, R. B., Clilverd, M. A., & Ross, J. P. J. (2019). An investigation of VLF transmitter wave power in the inner radiation belt and slot region. *Journal of Geophysical Research: Space Physics*, *124*, 5246–5259. <https://doi.org/10.1029/2019JA026715>
- Meredith, N. P., Horne, R. B., Glauert, S. A., & Anderson, R. R. (2007). Slot region electron loss timescales due to plasmaspheric hiss and lightning-generated whistlers. *Journal of Geophysical Research*, *112*, A08214. <https://doi.org/10.1029/2007JA012413>
- Meredith, N. P., Horne, R. B., Glauert, S. A., Baker, D. N., Kanekal, S. G., & Albert, J. M. (2009). Relativistic electron loss timescales in the slot region. *Journal of Geophysical Research*, *114*, A03222. <https://doi.org/10.1029/2008JA013889>
- Meredith, N. P., Horne, R. B., Kersten, T., Li, W., Bortnik, J., Sicard, A., & Yearby, K. H. (2018). Global model of plasmaspheric hiss from multiple satellite observations. *Journal of Geophysical Research: Space Physics*, *123*, 4526–4541. <https://doi.org/10.1029/2018JA025226>
- Meredith, N. P., Horne, R. B., Thorne, R. M., Summers, D., & Anderson, R. R. (2004). Substorm dependence of plasmaspheric hiss. *Journal of Geophysical Research*, *109*, A06209. <https://doi.org/10.1029/2004JA010387>
- Mourenas, D., Artemyev, A. V., Agapitov, O. V., & Krasnoselskikh, V. (2013). Analytical estimates of electron quasi-linear diffusion by fast magnetosonic waves. *Journal of Geophysical Research: Space Physics*, *118*, 3096–3112. <https://doi.org/10.1002/jgra.50349>
- Němec, F., Santolík, O., Gereová, K., Macúšová, E., de Conchy, Y., & Cornilleau-Wehrlin, N. (2005). Initial results of a survey of equatorial noise emissions observed by the cluster spacecraft. *Planetary and Space Science*, *53*(1), 291–298. <https://doi.org/10.1016/j.pss.2004.09.055>
- Olson, W., & Pfitzer, K. (1977). *Magnetospheric magnetic field modeling. Annual scientific report*. Air Force Office of Science Research.
- Ozhogin, P., Tu, J., Song, P., & Reinisch, B. W. (2012). Field-aligned distribution of the plasmaspheric electron density: An empirical model derived from the IMAGE RPI measurements. *Journal of Geophysical Research*, *117*, A06225. <https://doi.org/10.1029/2011JA017330>
- Perraut, S., Roux, A., Robert, P., Gendrin, R., Sauvaud, J.-A., Bosqued, J.-M., et al. (1982). A systematic study of ULF waves above F_{H^+} from GEOS 1 and 2 measurements and their relationships with proton ring distributions. *Journal of Geophysical Research*, *87*(A8), 6219–6236. <https://doi.org/10.1029/JA087iA08p06219>
- Ripoll, J.-F., Albert, J. M., & Cunningham, G. S. (2014). Electron lifetimes from narrowband wave–particle interactions within the plasmasphere. *Journal of Geophysical Research: Space Physics*, *119*, 8858–8880. <https://doi.org/10.1002/2014JA020217>
- Ross, J. P. J., Glauert, S. A., Horne, R. B., Watt, C. E. J., & Meredith, N. P. (2021). On the variability of emic waves and the consequences for the relativistic electron radiation belt population. *Journal of Geophysical Research: Space Physics*, *126*, e2021JA029754. <https://doi.org/10.1029/2021JA029754>
- Ross, J. P. J., Glauert, S. A., Horne, R. B., Watt, C. E., Meredith, N. P., & Woodfield, E. E. (2020). A new approach to constructing models of electron diffusion by emic waves in the radiation belts. *Geophysical Research Letters*, *47*, e2020GL088976. <https://doi.org/10.1029/2020GL088976>
- Ross, J. P. J., Meredith, N. P., Glauert, S. A., Horne, R. B., & Clilverd, M. A. (2019). Effects of VLF transmitter waves on the inner belt and slot region. *Journal of Geophysical Research: Space Physics*, *124*, 5260–5277. <https://doi.org/10.1029/2019JA026716>
- Russell, C. T., Holzer, R. E., & Smith, E. J. (1969). OGO 3 observations of ELF noise in the magnetosphere: I. Spatial extent and frequency of occurrence. *Journal of Geophysical Research*, *74*(3), 755–777. <https://doi.org/10.1029/JA074i003p0755>
- Santolík, O., Němec, F., Gereová, K., Macúšová, E., de Conchy, Y., & Cornilleau-Wehrlin, N. (2004). Systematic analysis of equatorial noise below the lower hybrid frequency. *Annales Geophysicae*, *22*(7), 2587–2595. <https://doi.org/10.5194/angeo-22-2587-2004>
- Santolík, O., Parrot, M., & Lefeuvre, F. (2003). Singular value decomposition methods for wave propagation analysis. *Radio Science*, *38*(1), 1010. <https://doi.org/10.1029/2000RS002523>
- Sheeley, B. W., Moldwin, M. B., Rassoul, H. K., & Anderson, R. R. (2001). An empirical plasmasphere and trough density model: CRRES observations. *Journal of Geophysical Research*, *106*(A11), 25631–25641. <https://doi.org/10.1029/2000JA000286>
- Shi, R., Summers, D., Ni, B., Fennell, J. F., Blake, J. B., Spence, H. E., & Reeves, G. D. (2016). Survey of radiation belt energetic electron pitch angle distributions based on the Van Allen Probes MagEIS measurements. *Journal of Geophysical Research: Space Physics*, *121*, 1078–1090. <https://doi.org/10.1002/2015JA021724>
- Shprits, Y. Y., Runov, A., & Ni, B. (2013). Gyro-resonant scattering of radiation belt electrons during the solar minimum by fast magnetosonic waves. *Journal of Geophysical Research: Space Physics*, *118*, 648–652. <https://doi.org/10.1002/jgra.50108>
- Tsyganenko, N. A., & Sitnov, M. I. (2005). Modeling the dynamics of the inner magnetosphere during strong geomagnetic storms. *Journal of Geophysical Research*, *110*, A03208. <https://doi.org/10.1029/2004JA010798>
- Van Allen, J. A. (1959). The geomagnetically trapped corpuscular radiation. *Journal of Geophysical Research*, *64*(11), 1683–1689. <https://doi.org/10.1029/JZ064i011p01683>
- Van Allen, J. A., & Frank, L. A. (1959). Radiation around the Earth to a radial distance of 107,400 km. *Nature*, *183*, 430–434. <https://doi.org/10.1038/183430a0>
- Watt, C. E. J., Allison, H. J., Meredith, N. P., Thompson, R. L., Bentley, S. N., Rae, I. J., et al. (2019). Variability of quasilinear diffusion coefficients for plasmaspheric hiss. *Journal of Geophysical Research: Space Physics*, *124*, 8488–8506. <https://doi.org/10.1029/2018JA026401>

- Wrenn, G. L. (1995). Conclusive evidence for internal dielectric charging anomalies on geosynchronous communications spacecraft. *Journal of Spacecraft and Rockets*, 32(3), 514–520. <https://doi.org/10.2514/3.26645>
- Wrenn, G. L., Rodgers, D. J., & Ryden, K. A. (2002). A solar cycle of spacecraft anomalies due to internal charging. *Annales Geophysicae*, 20(7), 953–956. <https://doi.org/10.5194/angeo-20-953-2002>
- Yuan, Z., Ouyang, Z., Yu, X., Huang, S., Yao, F., & Funsten, H. O. (2018). Global distribution of proton rings and associated magnetosonic wave instability in the inner magnetosphere. *Geophysical Research Letters*, 45, 10160–10166. <https://doi.org/10.1029/2018GL079999>
- Záhlava, J., Němec, F., Santolík, O., Kolmašová, I., Hospodarsky, G. B., Parrot, M., et al. (2019). Lightning contribution to overall whistler mode wave intensities in the plasmasphere. *Geophysical Research Letters*, 46, 8607–8616. <https://doi.org/10.1029/2019GL083918>
- Zou, Z., Zuo, P., Ni, B., Wei, F., Zhao, Z., Cao, X., et al. (2019). Wave normal angle distribution of fast magnetosonic waves: A survey of Van Allen Probes EMFISIS observations. *Journal of Geophysical Research: Space Physics*, 124, 5663–5674. <https://doi.org/10.1029/2019JA026556>